

# Variational algorithms to remove stationary noise. Applications to microscopy imaging.

Jérôme Fehrenbach, Pierre Weiss, and Corinne Lorenzo

**Abstract**—A framework and an algorithm are presented in order to remove stationary noise from images. This algorithm is called VSNR (Variational Stationary Noise Remover). It can be interpreted both as a restoration method in a Bayesian framework and as a cartoon+texture decomposition method. In numerous denoising applications the white noise assumption fails: structured patterns (e.g. stripes) appear in the images. The model described here addresses these cases. Applications are presented with images acquired using different modalities: scanning electron microscope, FIB-nanotomography, and an emerging fluorescence microscopy technique called SPIM (Selective Plane Illumination Microscope).

**Index Terms**—Stripe removal, stationary noise, non linear filtering, total variation, texture-geometry decomposition, convex optimization, primal-dual scheme, Atomic Force Microscope, Light Sheet Fluorescence Microscope, Scanning Electron Microscope, nanotomography.

## I. INTRODUCTION

Many imaging modalities tend to impair images with structured noise. For instance, stripes appear in images produced by recent microscopes such as Single Plane Illumination Microscope (SPIM) [12], Atomic Force Microscope (AFM), scanning electron microscopy (SEM) [7], [13], Synchrotron X-Ray Tomographic images, Focused Ion Beam nanotomography [16], or in remote sensing imaging such as MODerate-resolution Imaging Spectroradiometer (MODIS) images or digital elevation models [2], [5], [6]. Figure 1 shows examples of stripes in images obtained using different microscopy modalities.

The main purpose of this work is to propose a simple noise model which describes accurately the kind of distortions appearing in Figure 1. This statistical modeling allows to formulate the restoration problem in a Bayesian framework. It leads to the resolution of a large scale convex programming problem which is solved using recent advances in numerical optimization. We call our algorithm VSNR which stands for Variational Stationary Noise Remover.

As far as we know, few works address this restoration problem. Recently, [16] proposed a combined wavelet and Fourier method which allows to interpolate and restore wavelet coefficients impaired by stripes. In [7], a Fourier filtering is proposed, where noisy Fourier coefficients are first detected using statistical tests. Contrarily to our work, these approaches do not rely on a precise statistical modeling of the noise and incorporate prior information on the images only implicitly.

Jérôme Fehrenbach and Pierre Weiss are with IMT-UMR5219 and with ITAV-UMS3039, laboratories from Université de Toulouse and CNRS, Toulouse, France.

Corinne Lorenzo is with ITAV-UMS3039 (Université de Toulouse and CNRS).

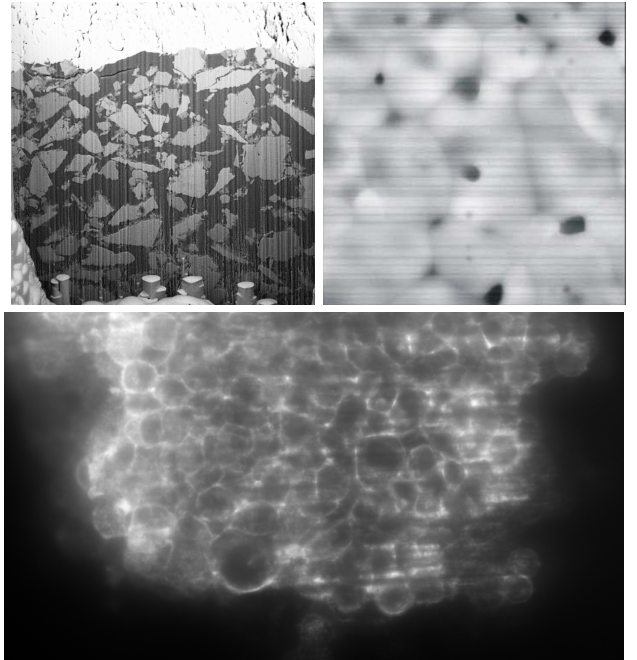


Fig. 1. Stripes for various imaging modalities. Top-left: cement paste image using Ion beam nanotomography. Top-right: sintered specimen of CeO<sub>2</sub> image using Scanning Electron Microscope (SEM). Bottom: medaka fish embryo image using Selective Plane Illumination Microscope (SPIM)

The image formation model we consider can be stated as follows:

$$u_0 = u + b$$

where  $u_0$  is the observed digital image and  $b$  is a noise or a texture. Our objective is to retrieve  $u$  knowing the observation  $u_0$ . A standard assumption in the literature is that the noise is white, meaning that the different components of  $b$  are independent random variables of finite variance. Though this noise assumption models accurately some real applications, it fails to do so in many scenarios. In the case of image restoration/denoising problems, it often leads to unsatisfactory results.

In this article we propose a noise model that suits more complex frameworks and that can be handled numerically in reasonable computing times. We replace the white noise assumption by a *stationary noise* assumption. A stationary noise  $b$  can be defined as a stochastic process having the following translation invariance property:

$$\forall \tau \in \mathbb{Z}^2, \quad \mathbf{p}(b) = \mathbf{p}(T_\tau(b)) \quad (1)$$

where  $\mathbf{p}$  denotes the probability density function and  $T_\tau$  is the translation of vector  $\tau$  with periodic boundary conditions on

the image domain. This hypothesis is natural in many applications, since it amounts to assume that there is no a-priori knowledge about the location of any feature or noise pattern in the image. However, the sole hypothesis of stationarity appears to be hardly numerically tractable. In this work, we restrict to a subclass of stationary stochastic processes, that can be easily described in the frequency domain: these processes are generated by convolving white noise with a given kernel. The noise thus appears as “structured” in the sense that some pattern might be visible, see Figure 3.

This model shares many similarities with the negative norm models of Y. Meyer [15], its successors [1] and the decomposition algorithms proposed in [10]. Meyer’s idea is to decompose an image into a piecewise smooth component and an oscillatory component. We refer to [1] for a review of the principles, algorithms and results using this approach. An alternative way of decomposing images was proposed in [10]. The idea is to seek for components that are sparse in given dictionaries. Different choices for the elementary atoms composing the dictionary allow to recover different kinds of textures.

The main contributions of the present paper are:

- 1) We propose a simple class of random processes that describes real-life noises and textures.
- 2) This approach generalizes the negative norm models proposed in [1], [15] in the discrete setting [11]. It allows more general noise priors than [10], which focuses on sparse models.
- 3) The decomposition problem is recast into a convex optimization problem that is solved with a recent algorithm of A. Chambolle and T. Pock [3] allowing to obtain results in an interactive time.
- 4) We propose a C and Matlab implementation on our webpage in the spirit of reproducible research <http://www.math.univ-toulouse.fr/~weiss/PageCodes.html>.

Moreover, a FIJI plugin will be available soon.

The outline of this paper is as follows. In section II, we introduce the notation. Section III contains definitions and some properties of the noise model. Section IV presents a restoration or decomposition model based on the maximum a posteriori (MAP) estimator. Section V details an efficient numerical scheme based on [3] to solve the resulting convex programming problems. In section VI we present some applications and results on synthetic and real images.

## II. NOTATION

In all the paper  $n = n_x \times n_y$  will refer to the number of pixels of the degraded image,  $m$  stands for the number of filters used to describe the noise. Let  $u \in \mathbb{R}^{n_x \times n_y}$  be an image,  $u(\mathbf{x})$  denotes the pixel of coordinates  $\mathbf{x} \in \{1, 2, \dots, n_x\} \times \{1, 2, \dots, n_y\}$ .

The standard  $\ell^p$ -norm of  $u$  is denoted  $\|u\|_p$ . Let  $u_1, u_2 \in \mathbb{R}^n$  the dot product is denoted  $\langle u_1, u_2 \rangle = u_1^T u_2$ .

Let  $\Lambda = \mathbb{R}^{n \times m}$  and  $Q = \mathbb{R}^{n \times 2}$ . An element  $\lambda \in \Lambda$  reads  $\lambda = \{\lambda_i\}_{i=1}^m$ . These spaces are endowed with inner products  $\langle \cdot, \cdot \rangle_\Lambda$  and  $\langle \cdot, \cdot \rangle_Q$ . We set  $\|q\|_Q = \sqrt{\langle q, q \rangle_Q}$  and  $\|\lambda\|_\Lambda = \sqrt{\langle \lambda, \lambda \rangle_\Lambda}$ .

Let  $A : \Lambda \rightarrow Q$  be a linear operator. The adjoint  $A^*$  of  $A$  is defined by:

$$\langle A\lambda, q \rangle_Q = \langle A^*q, \lambda \rangle_\Lambda, \quad \forall (\lambda, q) \in \Lambda \times Q.$$

The norm of the operator  $A$  is defined by:

$$\|A\| = \max_{\|\lambda\|_\Lambda \leq 1} \|A\lambda\|_Q.$$

The convolution operator with periodic boundary conditions is denoted  $*$ . The discrete Fourier and inverse Fourier transforms are respectively denoted  $\mathcal{F}$  and  $\mathcal{F}^{-1}$ . We will also use the notation  $\hat{u} = \mathcal{F}u$ . Finally,  $\nabla$  denotes the discrete gradient operator. In this article we use the following discretization:

$$\nabla u = (\partial_x u, \partial_y u)$$

where

$$\begin{aligned} (\partial_x u)(i, j) &= \begin{cases} u(i+1, j) - u(i, j) & \text{if } i < n_x \\ 0 & \text{if } i = n_x \end{cases} \\ (\partial_y u)(i, j) &= \begin{cases} u(i, j+1) - u(i, j) & \text{if } j < n_y \\ 0 & \text{if } j = n_y. \end{cases} \end{aligned}$$

Let  $\phi : \Lambda \rightarrow \mathbb{R} \cup \{+\infty\}$  be a convex, closed function. The domain of  $\phi$  is defined by  $\text{dom}(\phi) = \{\lambda \in \Lambda, \phi(\lambda) < +\infty\}$ .  $\phi^*$  refers to the Fenchel conjugate of  $\phi$  defined by:

$$\phi^*(\eta) = \sup_{\lambda \in \Lambda} \langle \eta, \lambda \rangle_\Lambda - \phi(\lambda). \quad (2)$$

The Fenchel conjugate satisfies  $\phi^{**} = \phi$ . Thus:

$$\phi(\lambda) = \sup_{\eta \in \Lambda} \langle \eta, \lambda \rangle_\Lambda - \phi^*(\eta). \quad (3)$$

The sub-differential of  $\phi$  at  $\lambda_1$  is the set defined by:

$$\partial\phi(\lambda_1) = \{\eta \in \Lambda, \phi(\lambda_2) \geq \phi(\lambda_1) + \langle \eta, \lambda_2 - \lambda_1 \rangle_\Lambda, \forall \lambda_2 \in \Lambda\}.$$

A function  $\phi$  is said to be strongly convex of parameter  $\gamma > 0$ , if the following inequality holds for all  $\lambda_1, \lambda_2 \in \text{dom}(\phi)$  and for all  $\eta \in \partial\phi(\lambda_1)$ :

$$\phi(\lambda_2) \geq \phi(\lambda_1) + \langle \eta, \lambda_2 - \lambda_1 \rangle_\Lambda + \frac{\gamma}{2} \|\lambda_2 - \lambda_1\|_\Lambda^2.$$

Let  $\Xi \subseteq \Lambda$  be a closed set. The indicator function of  $\Xi$  is denoted  $\chi_\Xi$  and defined by:

$$\chi_\Xi(x) = \begin{cases} 0 & \text{if } x \in \Xi \\ +\infty & \text{otherwise} \end{cases}.$$

The resolvent or proximal operator of  $\phi$  at  $\lambda$  is defined by:

$$(\text{Id} + \partial\phi)^{-1}(\lambda) = \arg \min_{\lambda' \in \Lambda} \phi(\lambda') + \frac{1}{2} \|\lambda' - \lambda\|_\Lambda^2.$$

It can be seen as a generalization of the projection operator since  $(\text{Id} + \partial\chi_\Xi)^{-1}(\lambda)$  is the projection of  $\lambda$  on the set  $\Xi$ . We refer to [9], [21] for a detailed presentation of the above tools.

### III. NOISE MODEL

In this paper, we consider the class of stationary processes (in the sense of (1)) that satisfy the following hypothesis:

*Hypothesis 3.1:* We assume that  $b$  reads:

$$b = \sum_{i=1}^m \lambda_i * \psi_i, \quad (4)$$

where:

- each  $\psi_i \in \mathbb{R}^n$  is a known elementary pattern,
- The  $\lambda_i$ 's are independent realizations of white noise processes with known probability density functions  $\mathbf{p}(\lambda_i)$ .

#### A. Rationale for the noise model

The images presented in Figure 1 are corrupted by parallel stripes. A noise removal algorithm should be able both to locate their position and to estimate their intensity. This perturbation can be modeled as  $b = \lambda * \psi$  where  $\psi$  is an elementary pattern, similar to a stripe, and  $\lambda$  describes the pattern positions and intensities.

In many applications, different kinds of noises or textures appear on the image simultaneously. For instance, in SPIM imaging in addition to stripes, Poisson or Gaussian white noise appears due to the imperfections of the imaging system. The Gaussian white noise can be obtained by convolving a Dirac function with a sample of white Gaussian noise. Setting  $m \geq 2$  in (4) thus allows to account for several noises.

#### B. Filters choice

The choice of filters  $\psi_i$  that appear in (4) depends on the application. For instance, in images obtained using pushbroom-type satellites [2], straight lines could be chosen. In microscopic images such as the ones presented in Figure 1 this model is not adapted: stripes usually have a finite extent and may be more than 1 pixel wide. The common feature of stripes in these images is their orientation  $\theta$ , as well as their size (width and length) that belong to a restricted range. In this paper, we model stripes as anisotropic Gaussian functions (see Figure 2) defined by:

$$\psi(x, y) = \exp\left(-\frac{x'^2}{\sigma_x^2} - \frac{y'^2}{\sigma_y^2}\right),$$

where  $x' = x \cos \theta + y \sin \theta$  and  $y' = -x \sin \theta + y \cos \theta$ . These functions have the advantage of being smooth both in space and frequency domain, this allows to account for inaccuracies between the noise model and the real noise.

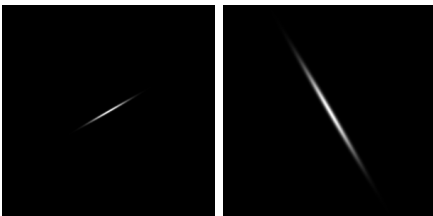


Fig. 2. Left: a Gaussian function in space domain – Right: the same Gaussian function in Fourier domain.

#### C. Distribution functions

The p.d.f.  $\mathbf{p}(\lambda_i)$  in equation (4) still needs to be defined. The p.d.f. should be chosen depending on the noise nature. In the experiments of this paper we consider three cases:

- *Uniform noise.* It is obtained by setting

$$\mathbf{p}(\lambda_i) \propto \begin{cases} 1 & \text{if } \|\lambda_i\|_\infty \leq \alpha_i \\ 0 & \text{otherwise.} \end{cases}$$

This assumption allows to model bounded noises. See right images in Figure 3.

- *Gaussian noise.* This hypothesis consists in setting  $\mathbf{p}(\lambda_i) \propto \exp(-\frac{\alpha_i}{2} \|\lambda_i\|_2^2)$ . The corresponding noise component  $b_i = \lambda_i * \psi_i$  is then a colored Gaussian noise. See middle images in Figure 3.
- *Laplace noise.* It is obtained by setting  $\mathbf{p}(\lambda_i) \propto \exp(-\alpha_i \|\lambda_i\|_1)$ . This distribution is a convex approximation of Bernoulli processes [8], [14]. See left images in Figure 3.

All these noise priors are generalized Gaussian distributions and their distribution function reads:

$$\mathbf{p}(\lambda_i) \propto \exp(-\phi_i(\lambda_i)) \text{ where } \phi_i: \mathbb{R}^n \rightarrow \mathbb{R} \cup \{+\infty\}. \quad (5)$$

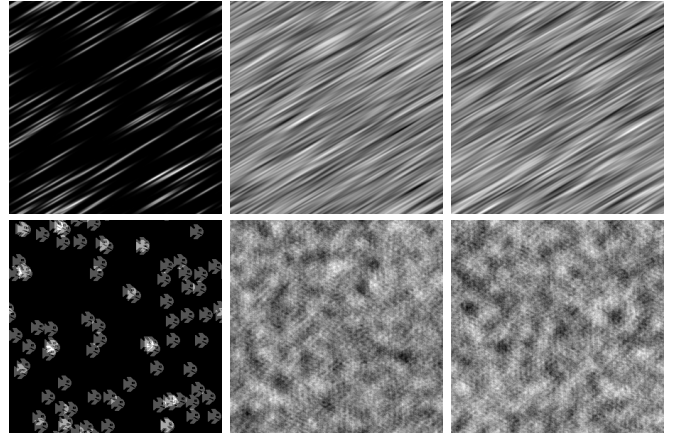


Fig. 3. Examples of stationary processes obtained by convolving white noises with different marginals with a filter. Top row: convolution with a Gaussian filter. Bottom row: convolution with a fish pattern. From left to right: convolution with a white Bernoulli process, a Gaussian white noise and a uniform white noise.

### IV. RESTORATION/DECOMPOSITION MODEL

Throughout this paper, we assume the following image formation model:

$$u_0 = u + b \quad (6)$$

where  $b$  is independent of  $u$  and satisfies Hypothesis 3.1.

#### A. A MAP reconstruction approach

In order to recover the noise components  $\lambda$  and the image  $u$ , the maximum a posteriori (MAP) approach leads to maximize:

$$\begin{aligned} \mathbf{p}(\lambda, u | u_0) &= \frac{\mathbf{p}(u_0 | \lambda, u) \mathbf{p}(\lambda, u)}{\mathbf{p}(u_0)} \\ &= \frac{\mathbf{p}(u_0 | \lambda, u) \mathbf{p}(\lambda) \mathbf{p}(u)}{\mathbf{p}(u_0)}. \end{aligned}$$

Taking the log of the conditional probability leads to the following optimization problem:

$$\text{Find } \lambda^* \in \underset{\lambda \in \Lambda}{\text{Arg min}} -\log \mathbf{p}(u_0|\lambda, u) - \log \mathbf{p}(\lambda) - \log \mathbf{p}(u). \quad (7)$$

As we assumed independence of the  $\lambda_i$ s,

$$-\log \mathbf{p}(\lambda) = \sum_{i=1}^m -\log \mathbf{p}(\lambda_i).$$

Moreover

$$\begin{aligned} \mathbf{p}(u_0|\lambda, u) &= \mathbf{p}\left(u + \sum_{i=1}^m \lambda_i * \psi_i | \lambda, u\right) \\ &= \delta\left(u + \sum_{i=1}^m \lambda_i * \psi_i - u_0\right), \end{aligned}$$

where  $\delta$  denotes the Dirac mass. In order to specify problem (7), we still need to define the image prior  $\mathbf{p}(u)$ .

*Remark 4.1:* In some applications the independence of  $u$  and  $\lambda$  is questionable and a multiplicative model could be considered. Our numerical experiments using multiplicative models did not improve the results sensibly compared to the additive models and required heavier computations.

### B. Image prior

In this work, we use the standard assumption that images are smooth or piecewise smooth. This can be promoted by a p.d.f. of the form

$$\mathbf{p}(u) \propto \exp(-\|\nabla u\|_{1,\epsilon}) \quad (8)$$

where

$$\begin{aligned} \|\cdot\|_{1,\epsilon} : \mathbb{R}^{n \times 2} &\rightarrow \mathbb{R} \\ q &\mapsto \|q\|_{1,\epsilon} = \sum_{\mathbf{x}} \phi_{\epsilon}(\|q(\mathbf{x})\|_2) \end{aligned}$$

and

$$\phi_{\epsilon}(t) = \begin{cases} \frac{t^2}{2\epsilon} & \text{if } |t| \leq \epsilon \\ |t| - \frac{\epsilon}{2} & \text{otherwise.} \end{cases}$$

This function can be rewritten using duality [24] as:

$$\|z\|_{1,\epsilon} := \max_{\|q\|_{\infty} \leq 1} \langle z, q \rangle - \frac{\epsilon}{2} \|q\|_2^2.$$

The interest of this prior is twofold:

- The standard isotropic  $\ell^1$ -norm  $\mathbb{R}^{n \times 2}$  corresponds to  $\|\cdot\|_{1,0}$  and  $\lim_{\epsilon \rightarrow +\infty} \epsilon \|\cdot\|_{1,\epsilon} = \|\cdot\|_2^2$ . This formalism thus captures the standard  $\ell^1$  (total variation) and  $\ell^2$  (Tikhonov) regularization.
- by setting  $\epsilon \neq 0$ , the numerical scheme designed to solve (7) converges faster than for  $\epsilon = 0$  and may provide better results in some applications.

### C. Resulting optimization problems

By replacing formulas (8) and (5) in (7) we obtain the following optimization problem:

$$\text{Find } \lambda \in \underset{\lambda \in \Lambda}{\text{Arg min}} P(\lambda), \quad (9)$$

where

$$P(\lambda) = \left\| \nabla \left( u_0 - \sum_{i=1}^m \lambda_i * \psi_i \right) \right\|_{1,\epsilon} + \sum_{i=1}^m \phi_{\epsilon}(\lambda_i).$$

## V. NUMERICAL ALGORITHMS

In the case of Tikhonov regularization (which corresponds to  $\phi_i(\lambda) = \frac{\alpha_i}{2} \|\lambda_i\|_2^2$  and  $\epsilon \gg 0$ ), Problem (9) can be solved exactly in  $O(m^3 n \log n)$  operations using Fourier transforms and inversion of small  $m \times m$  linear systems. In the general case, it is impossible to get an exact solution. The objective of this section is to design iterative methods that lead to approximate solutions of (9).

### A. Problem relaxation

Since problem (9) cannot be solved exactly, we are interested in finding an  $\epsilon$ -solution defined by:

$$\text{Find } \lambda_{\epsilon} \in \Lambda \text{ such that } P(\lambda_{\epsilon}) - P(\lambda^*) \leq \epsilon. \quad (10)$$

An iterative optimization algorithm defines a sequence  $(\lambda_k)_{k \in \mathbb{N}}$  that converges to a solution of (9). The resolution of (10) amounts to define an appropriate stopping criterion. Since  $P(\lambda^*)$  is unknown,  $P(\lambda_k) - P(\lambda^*)$  cannot be evaluated. However this quantity can be bounded by the duality gap defined in equation (15). In order to prevent the duality gap to be infinite (corresponding to an infeasible dual variable), we add a box constraint to problem (10). This extra constraint also allows to obtain convergence rates, see Proposition 5.3.

To summarize, the constrained problem we consider reads:

$$\text{Find } \lambda_{\epsilon} \in \Xi \text{ such that } P(\lambda_{\epsilon}) - P(\lambda^*) \leq \epsilon, \quad (11)$$

where

$$\Xi = \{ \lambda \in \mathbb{R}^{n \times m}, \|\lambda\|_{\infty} \leq C \},$$

$\lambda^*$  is one exact solution of (9) and  $C$  is large enough (e.g.  $C \geq \|\lambda^*\|_{\infty}$ ). Under the latter condition, the extra box-constraint is inactive at the minimizer and the solutions of (11) are the same as those of (10).

### B. Reformulation as a saddle-point problem

This section is devoted to the resolution of (11). In order to apply the ideas presented in [3], we reformulate (11) as a saddle-point problem.

To simplify the reading, let us first introduce some notation.  $A$  is the following linear operator:

$$\begin{aligned} A : \Lambda &\rightarrow Q \\ \lambda &\mapsto \nabla \left( \sum_{i=1}^m \lambda_i * \psi_i \right) \end{aligned} \quad (12)$$

By denoting

$$F(g) = \|\nabla u_0 - g\|_{1,\epsilon}$$

and

$$G(\lambda) = \sum_{i=1}^m \phi_{\epsilon}(\lambda_i) + \chi_{\Xi}(\lambda),$$

$P(\lambda)$  reduces to:

$$P(\lambda) = F(A\lambda) + G(\lambda).$$

Moreover using property (3), problem (11) can be recast as the following convex-concave saddle-point problem:

$$\min_{\lambda \in \Xi} \max_{q \in Q} \langle A\lambda, q \rangle_Q - F^*(q) + G(\lambda). \quad (13)$$

The interest of this saddle-point reformulation is twofold:

- It allows the use of primal-dual algorithms which are known as being robust and efficient.
- It allows to define a duality gap, which provides a reliable stopping criterion for the iterative algorithm. See point 4) of Theorem 5.1.

### C. Elementary properties of the problem

By inverting the minimum and the maximum in (13) we obtain the following dual problem:

$$\max_{q \in Q} D(q), \quad (14)$$

where

$$\begin{aligned} D(q) &= \min_{\lambda \in \Lambda} \langle A\lambda, q \rangle_Q - F^*(q) + G(\lambda) \\ &= -F^*(q) - G^*(-A^*q). \end{aligned}$$

The duality gap is defined as the difference between the primal function  $P$  and the dual function  $D$ :

$$\Delta(\lambda, q) = P(\lambda) - D(q). \quad (15)$$

The following theorem characterizes the solutions of problem (11).

*Theorem 5.1:*

- 1) Problem (11) admits a convex, non-empty set of solutions.
- 2) Problem (13) admits a non-empty set of saddle points.
- 3) Let  $(\lambda^*, q^*)$  be a saddle point of (13). It satisfies  $\Delta(\lambda^*, q^*) = 0$  and  $\lambda^*$  is a solution of problem (11).
- 4) For any  $(\lambda, q) \in \Xi \times \mathbb{R}^{n \times 2}$ ,  $\Delta(\lambda, q) \geq P(\lambda) - P(\lambda^*)$ .

*Proof:* Points (1) and (2) result from boundedness of the set  $\Xi \times \text{dom}(F^*)$  and convexity of the functionals. Points (3) and (4) are standard results of convex analysis [21]. ■

The following propositions will be useful in order to determine the algorithm step sizes.

*Proposition 5.1:* In the standard Euclidean metric, if  $\epsilon > 0$ , then  $F^*$  is strongly convex with parameter  $\epsilon$ .

*Proposition 5.2:* In the standard Euclidean metric, if  $\phi_i(\lambda_i) = \frac{\alpha_i}{2} \|\lambda_i\|_2^2$  for all  $i \in \{1..m\}$ , then  $G$  is strongly convex with parameter:

$$\gamma = \min_{i \in \{1..m\}} \alpha_i \quad (16)$$

### D. A primal-dual algorithm

Recently, Nesterov paved the way to the development of new efficient first order algorithms in [17], [20]. From a theoretical point of view, these algorithms are shown to be optimal in the class of first order methods and they outperform second order algorithms - like interior point methods - for large scale problems and moderate accuracy. Among all the papers published recently on this topic, [3] is probably the most versatile and we decided to present and implement this strategy. Applied to problem (11), this algorithm reads:

---

### Algorithm 1: Primal-Dual algorithm [3]

---

**Input:**

$\epsilon$ : the desired precision;

$(\bar{\lambda}_0, q_0)$ : a starting point;

$L = \|A\|$ ;

$\sigma_0, \tau_0$  such that  $\sigma_0 \tau_0 L^2 < 1$ ;

**Output:**

$\lambda_\epsilon$ : a solution to problem (11).

**begin**

$k=0$ ;

**while**  $\Delta(\lambda_k, q_k) > \epsilon \Delta(\lambda_0, q_0)$  **do**

$q_{k+1} = (\text{Id} + \sigma_k \partial F^*)^{-1}(q_k + \sigma_k A \bar{\lambda}_k)$

$\lambda_{k+1} = (\text{Id} + \tau_k \partial G)^{-1}(\lambda_k - \tau_k A^* q_{k+1})$

$(\tau_{k+1}, \sigma_{k+1}, \theta_k) = \text{Update}(\tau_k, \sigma_k, \epsilon, \gamma, L)$

$\bar{\lambda}_{k+1} = \lambda_{k+1} + \theta_k (\lambda_{k+1} - \lambda_k)$

$k = k + 1$ ;

**end**

**end**

---

The resolvents of  $F^*$  and  $G$  are calculated in Appendix A. Following [3], the Update function should be implemented according to the following rules:

---

### Algorithm 2: Step size update rules

---

**Input:**

$\epsilon$ : parameter of strong convexity of  $F^*$

$\gamma$ : parameter of strong convexity of  $G$  (see eq. (16))

$\sigma_k$  and  $\tau_k$ : step sizes at iteration  $k$

**Output:**  $\theta_k, \sigma_{k+1}$  and  $\tau_{k+1}$ .

**begin**

**if**  $\phi_i(\cdot) = \frac{\alpha_i}{2} \|\cdot\|_2^2$  for all  $i \in \{1..m\}$  **then**

**if**  $\epsilon > 0$  **then**

      The sequence  $((\tau_k, \sigma_k))_{k \in \mathbb{N}}$  is constant:

$\mu = 2\sqrt{\gamma\epsilon}/L$ ;

$\tau_{k+1} = \frac{\mu}{2\gamma}$ ;

$\sigma_{k+1} = \frac{\mu}{2\epsilon}$ ;

$\theta_k = \frac{1}{1+\mu}$

**else**

$\theta_k = \frac{1}{\sqrt{1+2\gamma\tau}}$ ;

$\tau_{k+1} = \theta_k \tau_k$ ;

$\sigma_{k+1} = \frac{\sigma_k}{\theta_k}$ ;

**end**

**else**

    The sequence  $((\tau_k, \sigma_k))_{k \in \mathbb{N}}$  is constant:

$\theta_k = 1$ ;  $\tau_{k+1} = \tau_k$

$\sigma_{k+1} = \sigma_k$

**end**

**end**

---

The convergence properties of this algorithm are summarized below.

*Proposition 5.3:* The sequence  $(\lambda_k, q_k)_{k \in \mathbb{N}}$  generated by Algorithm 1 converges to a saddle-point of (13). Moreover it guarantees the following convergence rates:

- If  $\epsilon = 0$  and a function  $\phi_i$  is non quadratic then:

$$\Delta(\lambda_k, q_k) = O\left(\frac{L}{k}\right)$$

- If  $\epsilon = 0$  and all functions  $\phi_i$  are squared  $\ell^2$ -norms:

$$\Delta(\lambda_k, q_k) = O\left(\frac{L}{k^2}\right)$$

and

$$\|\lambda_k - \lambda^*\|_2^2 = O\left(\frac{L^2}{k^2}\right)$$

- If  $\epsilon > 0$  and all functions  $\phi_i$  are  $\ell^2$ -norms, the convergence is at least linear:

$$\Delta(\lambda_k, q_k) = O\left(\omega^{k/2}\right)$$

and

$$\|\lambda_k - \lambda^*\|_2^2 = O\left(\omega^{k/2}\right)$$

$$\text{with } \omega = \frac{1}{1 + \frac{\sqrt{\gamma\epsilon}}{L}}.$$

The proof of this proposition is a straightforward application of results in [3].

*Remark 5.1:* As Chambolle-Pock's method is first-order, the algorithm depends on the choice of the inner products on the primal and dual spaces. It is possible to define different inner products  $\langle \cdot, \cdot \rangle_\Lambda$  and  $\langle \cdot, \cdot \rangle_Q$ , leading to different iterative methods. This remark can be used to precondition the problem and obtain faster convergence rates, see [4] and paragraph VI-C for more details.

## VI. RESULTS

In this section we first present experimental results on images impaired by synthetic noise. We perform comparisons between the proposed algorithm and two recent works dedicated to stripes removal [7], [16]. We also present an example where the noise is synthesized as the sum of  $m = 2$  stationary processes. This illustrates our algorithm's ability to cope with more complicated noises. We then present results on real images acquired using different modalities: FIB-nanotomography, SEM and SPIM. We finish the section by discussing the experimental convergence behavior of the algorithm.

### A. Synthetic noise examples

In order to evaluate the performance of the proposed algorithm, we synthesise noise according to model (4) and add it to Figure 4. In the first experiment, we consider  $m = 1$  noise component, the filter  $\psi_1$  is a straight vertical line running over the entire vertical direction and  $\lambda_1$  is the realization of a Gaussian white noise process with different variances. The noisy images are then restored using three algorithms: VSNR, the DeStripe algorithm available on <http://biodev.cea.fr/destripe/> [7], and the wavelet-FFT algorithm [16]. The wavelet-FFT algorithm implementation was kindly provided by Dr. Beat Münch as a Fiji plugin.

We compare the results of the different restoration algorithms using a rescaled SNR measure (denoted SNRr) defined as follows:

$$SNRr(u_0, u) = SNR(\tilde{u}_0, u) = 10 \log_{10} \left( \frac{\|u\|_2^2}{\|\tilde{u}_0 - u\|_2^2} \right)$$

where  $\tilde{u}_0 = au_0 - b$  and  $(a, b) = \arg \min_{(a,b) \in \mathbb{R}^2} \|au_0 - b - u\|_2^2$ .

This measure provides the best SNR among all possible affine transforms of the grey levels of  $u_0$ . We chose this measure since the wavelet-FFT algorithm tends to decrease the contrasts.

The results are shown in Table I and in Figure 5. VSNR outperforms the two other methods by a few dBs. Note that when the noise level is low (first line of Table I), both the DeStripe and wavelet-FFT methods tend to degrade images. This is due to the fact that the noise description is too rough and this affects signal recovery.



Fig. 4. Original pirate image.

In the second experiment, we consider  $m = 1$  noise component, the filter  $\psi_1$  is an elongated Gaussian and  $\lambda_1$  is the realization of a Gaussian white noise process with different variances. The results are shown in table II and in Figure 6. Once again, VSNR clearly outperforms the two other methods. Figure 6 shows that the algorithm recovers most of the signal even when the noise level is higher than the signal level.

TABLE I

SNRR OF THE IMAGES DENOISED USING DIFFERENT ALGORITHMS. THE NOISE IS OBTAINED BY CONVOLVING WHITE GAUSSIAN NOISE WITH A STRAIGHT LINE. THE THIRD LINE CORRESPONDS TO FIGURE 5.

Initial SNRr	DeStripe	Wavelet - FFT	VSNR
33.85	33.70	22.61	43.00
19.73	20.52	22.03	37.54
8.63	16.60	15.15	25.32

TABLE II

SNRR OF THE IMAGES DENOISED USING DIFFERENT ALGORITHMS. THE NOISE IS OBTAINED BY CONVOLVING WHITE GAUSSIAN NOISE WITH AN ELONGATED GAUSSIAN. THE THIRD LINE CORRESPONDS TO FIGURE 6.

Initial SNRr	DeStripe	Wavelet-FFT	VSNR
32.68	30.64	23.63	34.42
21.80	22.53	18.98	26.31
8.14	8.15	8.29	13.31

In the third experiment, we consider  $m = 2$  noise components, the first filter  $\psi_1$  is a radial *sinc* function, the second filter  $\psi_2$  is an elongated Gaussian in the vertical direction,  $\lambda_1$  is a sample of a white Gaussian process and  $\lambda_2$  is a sample of a white Bernoulli process with low probability. The noisy image is shown in Figure 7 and the decomposition result is shown in Figure 8.



Fig. 5. Top-left: noisy pirate. Top-right: denoised using VSNR. Bottom-left: denoised using DeStripe [7]. Bottom-right: denoised using Wavelet-FFT [16]. This experiment corresponds to the last line of Table I. The noise pattern is a vertical line. The DeStripe and Wavelet-FFT algorithms do not completely remove low frequencies while VSNR leads to near perfect results.

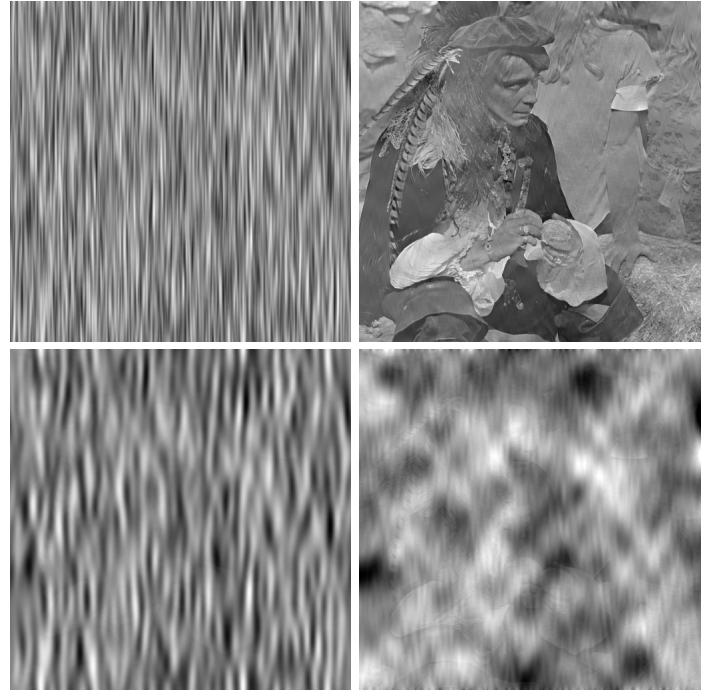


Fig. 6. Top-left: noisy pirate. Top-right: denoised using VSNR. Bottom-left: denoised using DeStripe [7]. Bottom-right: denoised using Wavelet-FFT [16]. This experiment illustrates the third line of Table II. In that example, the noise pattern is an elongated Gaussian in the vertical direction. The noise level is higher than the signal level. The VSNR algorithm retrieves most of the signal while the other two algorithms do not.

## B. Real images

In order to assess the efficiency of VSNR algorithm, we perform tests on images issued from different modalities:

- FIB-nanotomography. This image was used in [16]. Results are shown in Figure 9.
- SEM imaging. This image was used in [7]. Results are shown in Figure 11.
- SPIM imaging. Results are shown in Figure 12 and 10. The images come from a microscope prototype developed at ITAV-UMS3039 (CNRS).

In all experiments, algorithm 1 is applied with  $m = 2$  filters  $\psi_1$  and  $\psi_2$ . The first filter  $\psi_1$  is a Dirac (which allows the recovery of white noise), and the second filter  $\psi_2$  is an anisotropic Gabor filter with principal axis directed by the stripes (this orientation is determined by the user). Different parameters were tested for filter  $\psi_2$  and led to similar results, outlining the robustness of this approach with respect to the filter choice. Since no ground truth is available for these images, only visual inspection can help assessing the algorithm's performance. Let us discuss the results:

- Figure 9 and 11 show that VSNR is able to preserve the small image details and to remove the stripes and most of the white noise. The output of the wavelet-FFT and DeStripe algorithms are still impaired with low frequency striping and white noise.
- In Figure 12 only the cells contour is stained. The images are significantly denoised and small details are preserved. This is a particularly hard example since the images are not piecewise constant (i.e. the ideal images with bounded

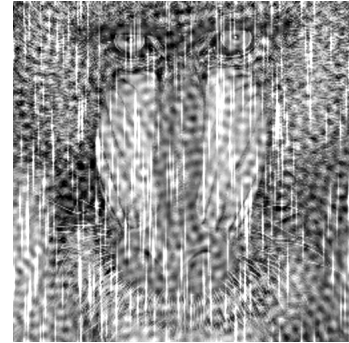


Fig. 7. Synthetic image used for the toy example. PSNR = 21.5dB.

variation).

- Figure 10 is a 3D visualisation of a stack, corresponding to a region of a multicellular tumor spheroid expressing a nuclear fluorescent protein, the H2B-HcRed. The 3D reconstruction of some objects (nuclei) performed by extraction of the isosurfaces of fluorescence intensity (in red, Imaris software) is substantially improved after processing.

## C. Numerical behavior

In this section, we briefly describe some aspects of the algorithm and of its numerical performance.

- Parameter tuning:* The convergence rates depend on the parameters in algorithm 1. There are at least 4 parameters that should be tuned:

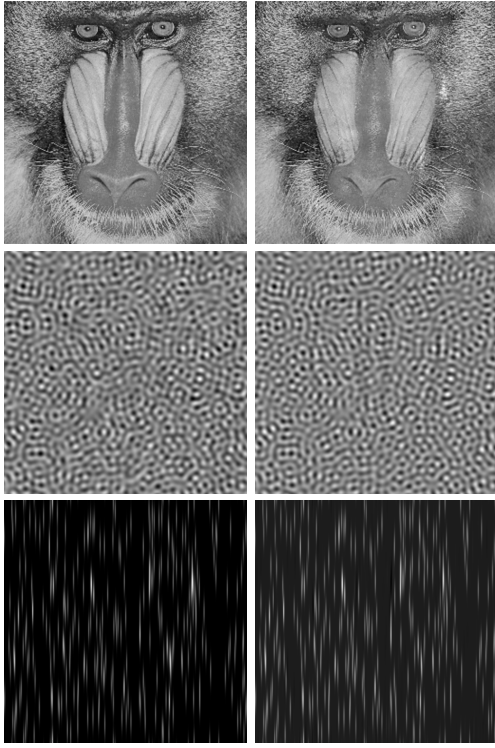


Fig. 8. Toy example. Left column: real components; right column: estimated components using our algorithm. Top: Baboon image (PSNR = 27dB) - Middle: Colored Gaussian noise (PSNR = 17.55dB) - Bottom: Impulse like noise (PSNR = 20.20dB)

- 1) First, it is important to have a tight estimate of  $L$ , the highest singular value of  $A$ , in order to choose  $\sigma$  and  $\tau$  as large as possible such that  $\sigma\tau L^2 < 1$ . An overestimation of  $L$  will slow down the scheme and an underestimation will make the scheme diverge. In the case of total variation, the calculation of  $L$  can be done explicitly, see Appendix B.
- 2) Second, the relationship  $\sigma\tau L^2 < 1$  still leaves a degree of freedom in the choice of  $\sigma$  and  $\tau$ . It is uneasy to choose these step sizes and it seems that only experimental tuning is available today.
- 3) Third, as stated in Remark 5.1, choosing different inner products in the primal space  $\Lambda$  and dual space  $Q$  will lead to different algorithms and can change the numerical performances of algorithm 1 drastically. This question is related to the previous one and we are currently conducting theoretical investigations in order to provide analytical solutions for these choices. A first answer was provided in [4].
- 4) Finally, it is important to have a reliable stopping criterion in order to automatize the algorithm. In all our experiments, choosing  $\epsilon = 10^{-3}$  as a stopping criterion in algorithm 1 led to solutions that were accurate enough for the visual system (no visible difference with the true solution). We believe that this is a very nice property of the proposed scheme as no user input is necessary.

b) *Analytical and empirical complexity:* The scheme's analytical complexity  $\mathcal{A}$  is given by:

$$\mathcal{A} = (\text{iterations number}) \times 2 \times m \times (\text{FFT}(n) + O(n) \text{ op.}) \\ + m \times \text{FFT}(n)$$

where  $n$  is the pixels number,  $m$  is the number of filters used in the model,  $\text{FFT}(n)$  indicates an FFT applied to a size  $n$  vector and op. means operations. This theoretical convergence rate indicates that the scheme is adapted to large scale problems: the dependence in  $n$  is just  $O(n \log(n))$ .

Our experiments showed that when the parameters in algorithm 1 are chosen correctly ( $\sigma$ ,  $\tau$  and the metrics), the scheme requires less than 50 iterations in order to decrease the initial duality gap by a factor  $\epsilon = 10^{-3}$ . The overall cost is thus around  $100 \times m$  FFT computations. The computational time is around 5 seconds for a  $1024 \times 1024$  image, on a 1.2GHz laptop, using  $m = 1$  filter.

A more formal complexity result could be obtained using the worst case convergence rates of the algorithm, but this rate seems to be always outperformed for the class of problems considered in this paper.

c) *A heuristic choice of the metrics:* All the tools used in algorithm 1 (Adjoints, singular values, Fenchel transforms, subgradients, proximal operators,...) depend on the choice of the inner products  $\langle \cdot, \cdot \rangle_\Lambda$  and  $\langle \cdot, \cdot \rangle_Q$ . In [4] some choices of the metrics are proposed in order to improve the convergence rates. In the present work, we simply rescaled the filters  $\psi_i$  and weights  $\alpha_i$ . This normalization is equivalent to a block-wise constant diagonal preconditionner.

## VII. CONCLUSION

We proposed a variational approach to denoise images impaired by a class of stationary noises. It takes advantage of recent advances in convex optimization, leading to interactive computing times. Applications to synthetic images, and to images issued from different microscopy imaging modalities were presented, leading to clear improvements of the image quality compared to existing methods.

### APPENDIX A

#### EXPLICIT EXPRESSIONS OF THE RESOLVENTS

In this section, we assume that  $\langle \cdot, \cdot \rangle_\Lambda$  and  $\langle \cdot, \cdot \rangle_Q$  are the standard dot products. The Fenchel conjugates  $F^*$  and  $G^*$  can be computed using Equation (2):

$$F^*(q) = \begin{cases} \frac{\epsilon}{2} \|q\|_2^2 - \langle \nabla u_0, q \rangle_Q & \text{if } \|q\|_\infty \leq 1 \\ +\infty & \text{otherwise} \end{cases}$$

and

$$G^*(\eta) = \sum_{i=1}^m (\phi_i + \chi_{[-C, C]^n})^*(\eta_i).$$

The adjoint of  $A$  is  $A^* = A^T$ , where:

$$A^T : \mathbb{R}^{n \times 2} \rightarrow \mathbb{R}^{m \times n} \\ q \mapsto (\nabla^T q * \check{\psi}_1, \dots, \nabla^T q * \check{\psi}_m)$$

and  $\check{\psi}_i = \mathcal{F}^{-1} \psi_i$ .

The different Fenchel transforms useful for the computation of  $G^*$  are:

- If  $\phi_i(\lambda) = \alpha_i \|\lambda\|_1$ :  
 $(\phi_i + \chi_{[-C, C]^n})^*(\eta) = C \|\max(0, |\eta| - \alpha_i)\|_1$ .
- If  $\phi_i(\lambda) = \frac{\alpha_i}{2} \|\lambda\|_2^2$ :  
 $(\phi_i + \chi_{[-C, C]^n})^*(\eta) = \alpha \left\| \min\left(\left|\frac{\eta}{\alpha}\right|, C\right) \left|\frac{\eta}{\alpha}\right| - \frac{1}{2} \min\left(\left|\frac{\eta}{\alpha}\right|, C\right)^2 \right\|_1$
- If  $\phi_i(\lambda) = \chi_{[-\alpha_i, \alpha_i]}(\lambda)$ :  
 $(\phi_i + \chi_{[-C, C]^n})^*(\eta) = \min(\alpha_i, C) \|\eta\|_1$

1) *Resolvent of  $F^*$* : Let us detail the calculation of:

$$q^* = (\text{Id} + \sigma \partial F^*)^{-1}(q_n) = \arg \min_{q \in \mathcal{Q}, \|q\|_\infty \leq 1} \frac{\sigma \epsilon}{2} \|q\|_2^2 - \langle \sigma \nabla u_0, q \rangle + \frac{1}{2} \|q - q_n\|_{\mathcal{Q}}^2. \quad (17)$$

Let

$$\tilde{q}_n = q_n + \sigma \nabla u_0.$$

By writing the Karush-Kuhn-Tucker optimality conditions, we obtain the following solution to problem (17):

$$q^*(\mathbf{x}) = \frac{\tilde{q}_n(\mathbf{x})}{\max(\|\tilde{q}_n(\mathbf{x})\|_2, \sigma \epsilon + 1)}$$

2) *Resolvent of  $G$* : In the second step of the algorithm, we must compute

$$\begin{aligned} \lambda^* &= (I + \tau \partial G)^{-1}(\lambda_n) \\ &= \arg \min_{\lambda \in \Lambda} \tau G(\lambda) + \frac{1}{2} \|\lambda - \lambda_n\|_\Lambda^2 \\ &= \arg \min_{\lambda \in \Xi} \sum_{i=1}^m \phi_i(\lambda_i) + \frac{1}{2\tau} \|\lambda_i - \lambda_{n,i}\|_{\Lambda_i}^2. \end{aligned}$$

As all the functions  $\phi_i$  are separable, this problem reduces to  $m \times n$  unidimensional problems of form:

$$\arg \min_{\lambda \in \mathbb{R}, |\lambda| \leq C} \tau f(\lambda) + \frac{1}{2} |\lambda - \lambda_n|^2 \quad (18)$$

where  $f$  is a convex function. In this work we focus on the cases:

- $f(\lambda) = \alpha |\lambda|$ .

The solution of (18) is given by:

$$\lambda^* = \frac{\max(|\lambda_n| - \tau \alpha, 0) \cdot \text{sign}(\lambda_n)}{\max(1, \max(|\lambda_n| - \tau \alpha, 0)/C)}.$$

- $f(\lambda) = \frac{\alpha}{2} \lambda^2$ .

The solution of (18) is given by:

$$\lambda^* = \frac{\frac{\lambda_n}{\tau \alpha + 1}}{\max(1, |\frac{\lambda_n}{\tau \alpha + 1}|/C)}.$$

- $f(\lambda) = \begin{cases} 0 & \text{if } |\lambda| \leq \alpha \\ +\infty & \text{otherwise} \end{cases}$

Let  $\delta = \min(C, \alpha)$ . The solution of (18) is given by:

$$\lambda^* = \frac{\lambda_n}{\max(1, |\lambda_n|/\delta)}.$$

## APPENDIX B

### COMPUTATION OF THE OPERATOR NORM $L$

It is important to use a tight estimation of  $L = \|A\|$ , the highest singular value of  $A$  defined in equation (12). In the case of total variation,  $L$  can be computed exactly if periodic boundary conditions are used to define the discrete gradient operator. With these boundary conditions, the discrete gradient operator  $\nabla = \begin{pmatrix} \partial_1 \\ \partial_2 \end{pmatrix}$  can be rewritten using convolution products and is thus diagonalized by the discrete Fourier transform (DFT):

$$\partial_1 u = d_1 * u = \mathcal{F}^{-1} \text{diag}(\hat{d}_1) \mathcal{F} u$$

and

$$\partial_2 u = d_2 * u = \mathcal{F}^{-1} \text{diag}(\hat{d}_2) \mathcal{F} u$$

where  $d_1$  and  $d_2$  are finite difference filters in the horizontal and vertical directions.

Let  $H_i$  be the matrix associated to the convolution product with  $\psi_i$ . It satisfies  $H_i \lambda_i = \psi_i * \lambda_i$  and is thus diagonalized by the DFT:

$$H_i = \mathcal{F}^{-1} \text{diag}(\hat{\psi}_i) \mathcal{F}.$$

Let us denote  $D_i = \text{diag}(\hat{d}_i)$ ,  $|D_i|^2 = \bar{D}_i D_i$  where  $\bar{D}_i$  is the complex conjugate of  $D_i$  and  $\Sigma = \sum_{i=1}^m \text{diag}(|\hat{\psi}_i|^2)$ . Elementary calculus then leads to:

$$AA^T = \begin{bmatrix} \mathcal{F}^{-1} & 0 \\ 0 & \mathcal{F}^{-1} \end{bmatrix} \cdot \begin{bmatrix} |D_1|^2 \Sigma & D_1 \Sigma D_2^* \\ D_2 \Sigma D_1^* & |D_2|^2 \Sigma \end{bmatrix} \cdot \begin{bmatrix} \mathcal{F} & 0 \\ 0 & \mathcal{F} \end{bmatrix}.$$

The eigenvalues of  $AA^T$  are the same as those of

$$\begin{bmatrix} |D_1|^2 \Sigma & D_1 \Sigma D_2^* \\ D_2 \Sigma D_1^* & |D_2|^2 \Sigma \end{bmatrix}.$$

This matrix is symmetric, positive, semi-definite and is constituted of four diagonal blocks.  $L$  is thus given by the maximum largest eigenvalue of the following  $n, 2 \times 2$  matrices:

$$M(\mathbf{k}) = \begin{bmatrix} |\hat{d}_1(\mathbf{k})|^2 \Sigma(\mathbf{k}) & \hat{d}_1(\mathbf{k}) \overline{\hat{d}_2(\mathbf{k})} \Sigma(\mathbf{k}) \\ \overline{\hat{d}_1(\mathbf{k})} \hat{d}_2(\mathbf{k}) \Sigma(\mathbf{k}) & |\hat{d}_2(\mathbf{k})|^2 \Sigma(\mathbf{k}) \end{bmatrix},$$

where  $\mathbf{k}$  belongs to the frequency domain and  $\Sigma(\mathbf{k}) = \sum_{i=1}^m \text{diag}(|\hat{\psi}_i(\mathbf{k})|^2)$ . This computation is achieved in  $O(n \log n)$  arithmetic operations.

## ACKNOWLEDGMENT

The authors would like to thank Bernard Ducommun, Raphaël Jorand and Valérie Lobjois from the IP3D team in Toulouse cancéropole for their tireless support during this work and for all SPIM related questions. They also thank François De Vieilleville for fruitful discussions. They thank Beat Münch for providing a Fiji implementation of the

Wavelet-FFT algorithm and test images, Jean-Luc Pellequer for the DeStripe algorithm and Renaud Podor for providing us the SEM image. J.F. was partly supported by a grant from CNRS.

## REFERENCES

- [1] J.-F. Aujol, G. Gilboa, T. Chan, and S. Osher, "Structure-Texture Image Decomposition - Modeling, Algorithms, and Parameter Selection," *International Journal of Computer Vision*, vol. 67, no. 1, pp. 111–136, April 2006.
- [2] H. Carfantan and J. Idier, "Statistical linear destriping of satellite-based pushbroom-type images," *IEEE Transactions on Geoscience and Remote Sensing*, 48,1860–1871, 2010.
- [3] A. Chambolle and T. Pock, "A first-order primal-dual algorithm for convex problems with applications to imaging," *J. Mathematical Imaging and Vision*, vol. 40, no.1, pp. 120–145, 2011.
- [4] T. Pock and A. Chambolle, "Diagonal preconditioning for first order primal-dual algorithms in convex optimization," *ICCV*, 2011.
- [5] J. Chen, Y. Shao, H. Guo, W. Wang, B. Zhu, "Destriping CMODIS Data by Power Filtering," *IEEE Trans. Geosci. Remote Sens.* vol. 41, pp. 2119–2124, 2003.
- [6] J. Chen, H. Lin, Y. Shao, L. Yang, "Oblique Striping Removal in Remote Sensing Imagery Based on Wavelet Transform," *Int. J. Remote Sens.* vol. 27, pp. 1717–1723, 2006.
- [7] S. Chen and J.L. Pellequer, "DeStripe: frequency-based algorithm for removing stripe noises from AFM images" *BMC Structural Biology*, vol. 11, no.7, 2011.
- [8] S.S. Chen, D.L. Donoho and M.A. Saunders, "Atomic decomposition by basis pursuit", *SIAM review*, 129–159, 2001.
- [9] H.H. Bauschke, P.L. Combettes, "Convex Analysis and Monotone Operator Theory in Hilbert Spaces", Springer Verlag, 2011.
- [10] M.J. Fadili, J.-L. Starck, J. Bobin, Y. Moudden, "Image decomposition and separation using sparse representations: an overview," *Proc. of the IEEE, Special Issue: Applications of Sparse Representation*, vol. 98, no. 6, pp. 983–994, 2010.
- [11] J. Fehrenbach, P. Weiss and C. Lorenzo, "Variational algorithms to remove stripes: a generalization of the negative norm models," *Proc. ICPRAM*, 2012.
- [12] J. Huisken, J. Swoger, F. Del Bene, J. Wittbrodt, and E. Stelzer, "Optical Sectioning Deep Inside Live Embryos by Selective Plane Illumination Microscopy," *Science*, vol. 305, no. 5686, pp. 1007–1009, 2004.
- [13] F. Kienberger, VP Pastushenko, G. Kada, T. Puntheeranurak, L. Chtcheglova, C. Riethmueller, C. Rankl, A. Ebner, P. Hinterdorfer I "Improving the contrast of topographical AFM images by a simple averaging filter," *Ultramicroscopy*, vol. 106, pp. 822–828, 2006.
- [14] S. Mallat, "A Wavelet Tour of Signal Processing: The Sparse Way," 2008, Academic Press.
- [15] Y. Meyer, "Oscillating Patterns in Image Processing and Nonlinear Evolution Equations," The Fifteenth Dean Jacqueline B. Lewis Memorial Lectures, American Mathematical Society, Boston, MA, 2001
- [16] B. Münch, P. Trtik, F. Marone, M. Stampanoni "Stripe and ring artifact removal with combined wavelet-Fourier filtering," *Opt. Express*, vol. 17, pp. 8568–8591, 2009.
- [17] A. Nemirovski, "Information-based complexity of linear operator equations," *Journal of Complexity*, vol. 8, pp. 153–175, 1992.
- [18] A. Nemirovski, "Prox-method with rate of convergence  $O(1/t)$  for variational inequalities with Lipschitz continuous monotone operators and smooth convex-concave saddle point problems," *SIAM J. Optimization*, vol. 15, no. 1, pp. 229–251, 2005.
- [19] Y. Nesterov, *Introductory Lectures on Convex Optimization: A Basic Course*, Kluwer Academic Publishers, 2004.
- [20] Y. Nesterov, "Smooth minimization of non-smooth functions," *Mathematical Programming*, vol. 103, no. 1, pp. 127–152, 2005.
- [21] R.T. Rockafellar, *Convex Analysis*, Princeton University Press 1970.
- [22] A. Shiryayev, *Probability Second Edition*, Springer, Graduate in Mathematics 95.
- [23] J.-B. Hiriart-Urruty and C. Lemarechal, "Convex Analysis and Minimization Algorithms", Vol. 2, Springer Verlag, Berlin, Germany, 1993
- [24] P. Weiss, L. Blanc-Féraud and G. Aubert, *Efficient schemes for total variation minimization under constraints in image processing*, *SIAM Journal on Scientific Computing*, 31, 3, 2047–2080, 2009.



**Jérôme Fehrenbach** received the PhD degree in mathematics from University of Nice-Sophia Antipolis in 1998. He serves as an associate professor at Institut de Mathématiques de Toulouse - UMR5219 in France. He is also a member of ITAV - UMS3039. His current research interest are inverse problems and image processing.



**Pierre Weiss** graduated from INSA de Toulouse in 2004. He received a PhD degree in signal processing from the University of Nice-Sophia Antipolis in 2008 and did a post-doc at Hong Kong Baptist University in 2009. Since 2010, he serves as an associate professor at INSA de Toulouse and is a member of Institut de Mathématiques de Toulouse - UMR5219. He is also a member of ITAV-UMS3039. His research interests are in the field of imaging and applied mathematics. It includes inverse problems, convex optimization and variational methods applied

to topics as image restoration, change detection, MRI or SPIM.



**Corinne Lorenzo**, PhD, graduated from the university of Toulouse in 2004. She is a member of IP3D group, ITAV-UMS3039 (Toulouse, France) and she is in charge of the SPIM imaging development.

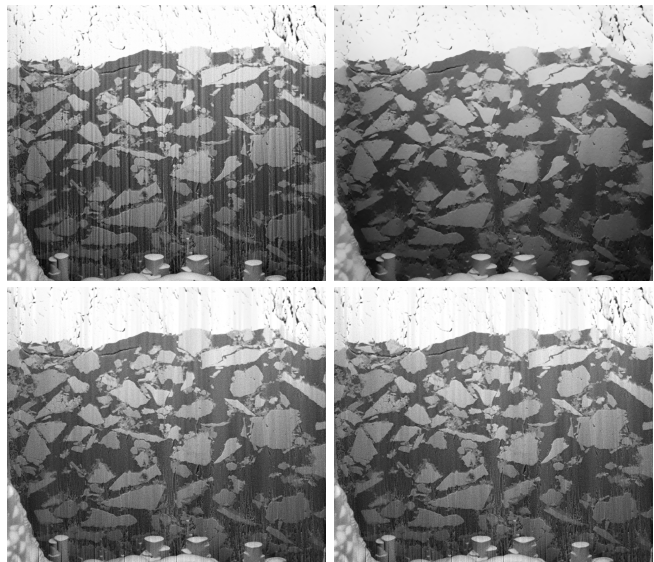


Fig. 9. Destriping of a single section from a 3D volume of unhydrated particles of cement paste accessed by FIB-nanotomography. Top-Left: original image is severely affected by the waterfall effect. Top-right: restored image using VSNR. Bottom-left: restored image using wavelet-FFT. Bottom-right: restored image using DeStripe.

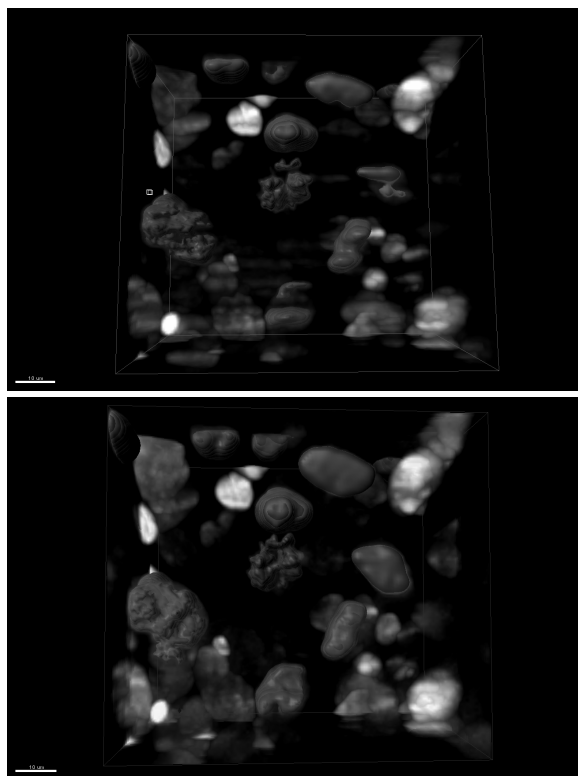


Fig. 10. Isosurface rendering (in red) of a three-dimensional stack of 42 planes of a Multicellular Tumor Spheroid expressing a fluorescent nuclear protein, H2B-HcRed. SPIM images were acquired with an objective 10X NA 0.25, an excitation wavelength of 595 nm and a detection using a 593 nm long pass filter. Top: raw data. Bottom: denoised data. The voxel size is  $0.645 \times 0.645 \times 1 \mu\text{m}$ .

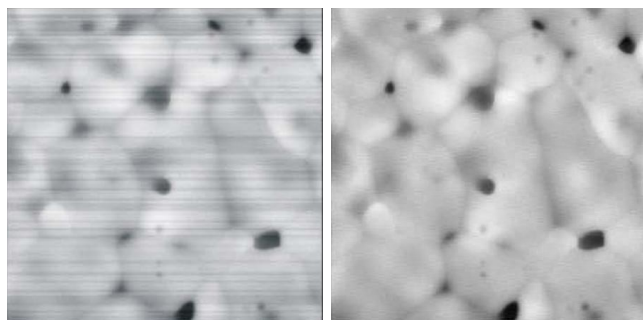


Fig. 11. SEM imaging on a sintered specimen of CeO<sub>2</sub> (cerium oxide) at a sintering temperature of 1400 C for 2 hours and 50 minutes [7]. The image is composed of 512x512 pixels with each side measuring 70.55  $\mu\text{m}$ ; the intensity unit is 0.1  $\mu\text{m}$ .

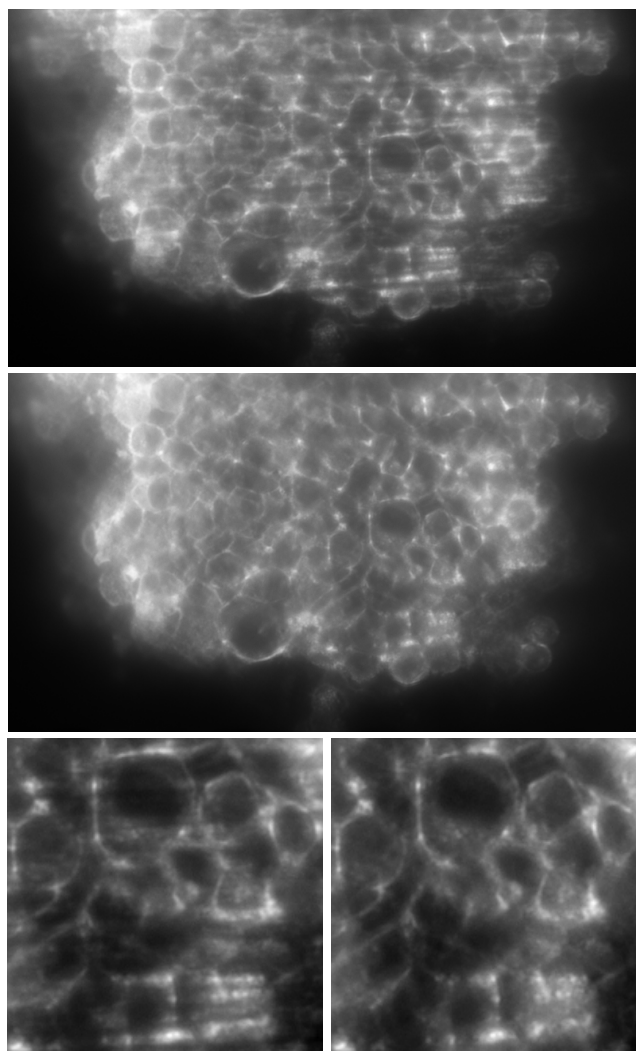


Fig. 12. SPIM images of a Multicellular Tumor Spheroid stained with DiI acquired with an objective 20X NA 0.5, an excitation wavelength of 532 nm and an emission wavelength of 593 nm. The voxel size is  $0.32 \times 0.32 \times 1 \mu\text{m}$ . Top: Single plane of a 3D stack; Middle: Denoised image using VSNR. Bottom: magnified views of a small region. Left: original, right: denoised.